High-Fidelity State Preparation, Quantum Control, and Readout of an Isotopically Enriched Silicon Spin Qubit

A.R. Mills,[1] C.R. Guinn,[1] M.M. Feldman,[1] A.J. Sigillito,[1,†] M.J. Gullans,[2] M.T. Rakher,[3] J. Kerckhoff,[3] C.A.C. Jackson,[3] and J.R. Petta[1,3,4,5,*]

[1] *Department of Physics, Princeton University, Princeton, New Jersey 08544, USA*

[2] *Joint Center for Quantum Information and Computer Science, NIST/University of Maryland, College Park, Maryland 20742, USA*

[3] *HRL Laboratories, LLC, 3011 Malibu Canyon Road, Malibu, California 90265, USA*

[4] *Department of Physics and Astronomy, University of California, Los Angeles, Los Angeles, California 90095, USA*

[5] *Center for Quantum Science and Engineering, University of California, Los Angeles, Los Angeles, California 90095, USA*

(Received 20 April 2022; revised 21 September 2022; accepted 15 November 2022; published 12 December 2022)

Quantum systems must be prepared, controlled, and measured with high fidelity in order to perform complex quantum algorithms. Control fidelities have greatly improved in silicon spin qubits but state-preparation and readout fidelities have generally been poor. By operating with low electron temperatures and employing high-bandwidth cryogenic amplifiers, we demonstrate single-qubit readout visibilities $> 99\%$, exceeding the threshold for quantum error correction. In the same device, we achieve average single-qubit control fidelities $> 99.95\%$. Our results show that silicon spin qubits can be operated with high overall operation fidelity.

DOI: 10.1103/PhysRevApplied.18.064028

I. INTRODUCTION

Backed by the highly successful semiconductor industry, the silicon spin-qubit platform provides the potential to scale to large system sizes and integrate the classical control circuitry necessary for advanced operation protocols [1–4]. Since the earliest demonstrations of spin-qubit logic in GaAs [5,6], a migration to isotopically enriched silicon [7] combined with improvements in $Si/(Si_{0.7}Ge_{0.3})$ heterostructure growth and device designs [8,9] have led to a recent surge of demonstrations of single- and two-qubit gates with fidelities above 99% [10–13].

In order for a qubit platform to be a serious contender for quantum information processing, it must be able to demonstrate all of the DiVincenzo criteria for quantum computing with high fidelity. While single- and two-qubit gates implemented in Si have made steady progress, state-preparation-and-measurement (SPAM) fidelities have generally been well below 90%, with a few recent exceptions [13–16]. To implement quantum error correction and realize fault-tolerant operation, the total logical error rate, which includes SPAM, must be kept low, at $\lesssim 2\%$ [17].

Depending on the qubit encoding, there are various protocols for initializing and reading out spin qubits [15,18] and a combination of techniques will likely be required for larger spin-qubit systems. Currently, readout in singlet-triplet and exchange-only qubits is performed using Pauli spin blockade [5,19], whereas single-spin qubits typically use Elzerman readout. The Elzerman approach utilizes state-dependent tunneling to prepare and measure spin qubits [20]. Protocols taking advantage of enhanced spin-charge relaxation in double quantum dots (DQDs) can be used to accelerate spin initialization or implement spin initialization in isolated DQDs that are not strongly tunnel coupled to leads [21,22]. Finally, there are a variety of schemes to improve the signal-to-noise-ratio (SNR) and measurement bandwidth through the use of cryogenic amplifiers [23], rf reflectometry [24], and latched charge and spin readout techniques [25–27].

In this paper, we demonstrate a readout visibility greater than 99% and average single-qubit gate fidelities above 99.95% in a single-spin Loss-DiVincenzo (LD) qubit. Cryogenic amplifiers and circuit optimization allow for low-noise high-bandwidth (1-MHz) charge sensing with a charge-detection SNR > 12. This high SNR, when combined with optimized spin-readout parameters, enables high-visibility Elzerman spin-state readout [20]. High-fidelity single-spin rotations in the same spin qubit are achieved using electric dipole spin resonance [28], as

*petta@physics.ucla.edu

†Department of Electrical and Systems Engineering, University of Pennsylvania, Philadelphia, Pennsylvania 19104, USA

verified by interleaved randomized benchmarking (IRB) [29]. These results show that overall operation fidelities in Si spin qubits can exceed important thresholds for fault-tolerant operation.

The device consists of a Si/($Si_{0.7}Ge_{0.3}$) heterostructure with an isotopically purified ^{28}Si (800 parts per million residual ^{29}Si) quantum well. Lithographically defined overlapping aluminum gate electrodes are used to define a linear array of six quantum dots with two proximal charge sensors [9]. High-fidelity state preparation, control, and measurement are demonstrated in a single LD qubit formed under gate P2 and a proximal charge detector S1 is used to read out the charge state of the quantum dot [Fig. 1(a)]. Microwaves are applied to the center MW gate to perform single-qubit rotations using electric dipole spin resonance in the field gradient of a Co micromagnet [28]. Dot 1 is kept empty ($N_1 = 0$) for these experiments and dot 2 is coupled to the reservoir via an accumulated channel on the right side of the device [9].

Spins are selectively prepared and measured using spin-to-charge conversion [20]. To obtain a 99% readout visibility, both electrical detection and spin-to-charge conversion have to function with high fidelity. For high-fidelity electrical detection, the measurement noise needs to be much lower than the charge-sensing signal associated with the spin-dependent tunneling events. As we demonstrate, robust charge sensing is feasible in Si spin-qubit devices and is generally not the limiting factor in the overall readout visibility. On the other hand, the tunnel rates, magnetic field, readout bias point, and signal sampling rate must be carefully optimized. The requirements for spin-to-charge conversion with visibility exceeding 99% are reviewed thoroughly by Keith *et al.* [30]. For each condition, the minimum requirements for achieving 99% visibility are as follows: (1) a large Zeeman splitting E_Z relative to the electron temperature T_e, $E_Z \gtrsim 13 k_B T_e$; (2) a fast tunnel-out time $t_{\rm out}^{\uparrow}$ for a spin-up electron relative to the spin-relaxation time T_1, $T_1 \gtrsim 100 t_{\rm out}^{\uparrow}$; and (3) a fast sampling rate Γ_s relative to the reload rate $1/t_{\rm in}^{\downarrow}$, $\Gamma_s \gtrsim 12/t_{\rm in}^{\downarrow}$. If any of these requirements are not met, 99% visibility Elzerman spin readout is not possible [30]. However, just barely meeting all of these requirements will also result in $< 99\%$ visibility. In practice, these three conditions must be budgeted such that the combined infidelities are $< 1\%$, as discussed below.

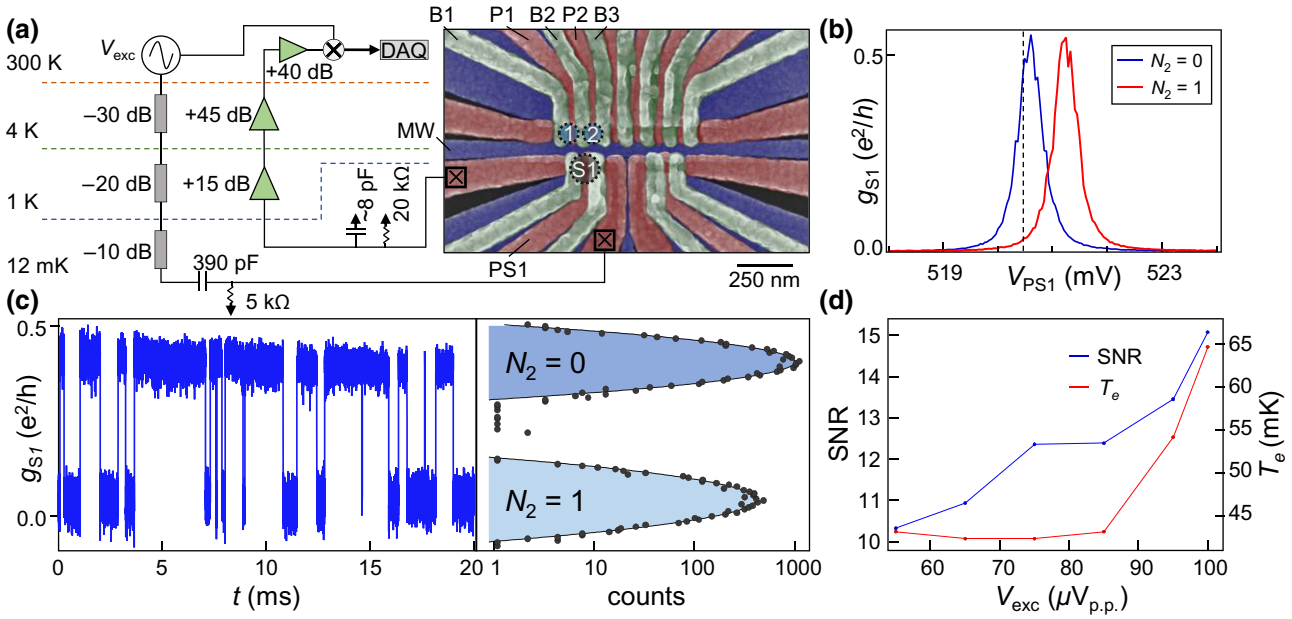

FIG. 1. High-fidelity charge-state determination. (a) A false-color scanning-electron-microscope image of the device, showing the two quantum dots and the charge sensor "S1" utilized for spin-to-charge conversion. The illustration to the left shows the charge-sensing circuit. An ac signal $V_{\rm exc}$ is highly attenuated before being ac coupled to the sensor dot. Two HEMT amplifiers measure the voltage drop across a 20-kΩ resistor that is mounted on the sample holder. Parasitic capacitance before the first-stage amplifier is indicated alongside the surface-mounted resistor. The signal is further amplified at room temperature before demodulation and digitization (DAQ). (b) A large shift of the sensor-dot Coulomb-blockade peak is evident when the occupancy of dot 2 changes from $N_2 = 0$ to $N_2 = 1$. The sensor bias point is indicated with a dashed line. (c) The time series of the charge-sensor conductance $g_{\rm S1}$ sampled at 1 mega-samples/s and with $V_{\rm exc} = 85 \mu V_{\rm p.p.}$, showing real-time tunneling events between $N_2 = 0$ and $N_2 = 1$ (left). The histogram of the time-series data used to extract the charge-readout SNR (right). (d) The charge-readout SNR and electron temperature T_e for dot 2, measured as a function of $V_{\rm exc}$.

II. OPTIMIZING MEASUREMENT FIDELITY

We first optimize the charge-state readout using the circuit shown in Fig. 1(a). A 1-MHz sine wave is applied to S1 and the drain current flows to ground through a 20-kΩ resistor. The voltage drop across the 20-kΩ resistor is amplified at the 1 K still plate (+15 dB gain) and the 4 K plate (+45 dB gain) before reaching a room-temperature amplifier [15]. The signal is then demodulated and digitized. Before the first-stage amplifier, there is approximately 8 pF of parasitic capacitance, which limits the circuit bandwidth to approximately 1 MHz. Figure 1(b) shows a Coulomb-blockade peak in the charge-sensor conductance g_{S1} as the sensor-dot plunger gate voltage, V_{PS1}, is swept. Changing the electron number in dot 2 from $N_2 = 0$ to $N_2 = 1$ shifts the Coulomb-blockade peak by approximately its full width at half maximum. When biased on the side of a Coulomb-blockade peak, the sensor dot can easily detect real-time tunneling events, as we now demonstrate.

High-bandwidth charge detection is illustrated in Fig. 1(c), where we show a time series of g_{S1} sampled at 1 mega-samples/s with the chemical potential of dot 2 tuned close to the Fermi level of the reservoir. Real-time tunneling events between the $N_2 = 0$ and $N_2 = 1$ charge states are visible. The switching rate between these charge states is set by the tunnel coupling Γ between the dot and the reservoir, tuned here to be slower than our measurement bandwidth. A histogram of these data is fitted by a double-Gaussian curve with center positions μ_n and standard deviations σ_n. The charge-readout SNR is set by the separation of the two Gaussians relative to their spread: $\mathrm{SNR} = (\mu_2 - \mu_1)/(\bar{\sigma})$, where we use $\bar{\sigma} = (\sigma_1 + \sigma_2)/2$ to account for slightly different standard deviations in the double-Gaussian.

Heating from the charge sensor is explored in Fig. 1(d), where we plot the SNR and electron temperature T_e as a function of the peak-to-peak excitation voltage V_{exc} at the sensor. The SNR increases with V_{exc} as expected but for $V_{\mathrm{exc}} > 85\mu V_{\mathrm{p.p.}}$ a steady increase of T_e with V_{exc} is observed. We therefore operate with $V_{\mathrm{exc}} = 85\mu V_{\mathrm{p.p.}}$, where the SNR is approximately 12.5 and $T_e \approx 45$ mK. This SNR corresponds to a lower-bound estimate of the charge-state infidelity $1 - F_c \geq 3 \times 10^{-10}$, which implies that our overall readout performance will be limited by the spin-to-charge conversion process [15]. We now explore the parameters that must be optimized for high-fidelity spin-to-charge conversion.

Figure 2(a) illustrates the process of spin-to-charge conversion for a spin-up electron. During the readout phase of an experiment, the energy of the spin-up and spin-down states of the quantum dot electron is set to straddle the Fermi level of the reservoir. The spin-up electron tunnels off the dot on a time scale set by $1/\Gamma^{\uparrow}_{\mathrm{out}}$ and is then replaced by a spin-down electron that tunnels into the dot on a time

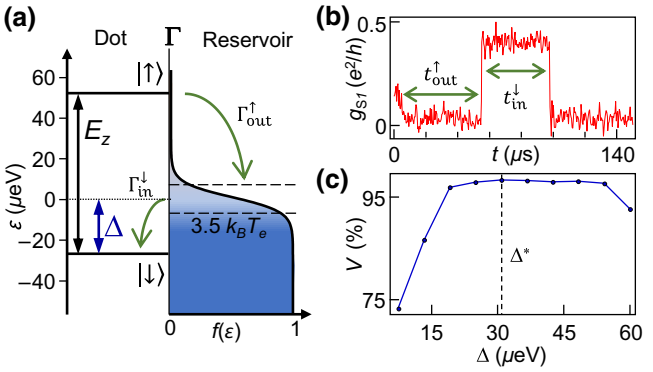

FIG. 2. The optimization of the physical readout parameters. (a) Quantum dot energy levels tunnel coupled to a thermally broadened Fermi reservoir. (b) The time series of a typical spin-up detection event, showing the measured tunneling times $t^{\downarrow}_{\mathrm{in}}(t^{\uparrow}_{\mathrm{out}})$ that are used to estimate the rates $\Gamma^{\downarrow}_{\mathrm{in}}(\Gamma^{\uparrow}_{\mathrm{out}})$. (c) The measurement visibility V as a function of the Fermi offset Δ. The offset Δ^* that maximizes V is then used in subsequent measurements.

scale set by $1/\Gamma^{\downarrow}_{\mathrm{in}}$ [20]. This sequence of events creates a detectable "spin bump" in the charge-sensing signal [see Fig. 2(b)]. $\Gamma^{\uparrow}_{\mathrm{out}}$ should be fast compared with the spin-relaxation rate $1/T_1$ but the reload rate $\Gamma^{\downarrow}_{\mathrm{in}}$ must be slow enough to allow the short change in electron occupancy to be detectable given the finite bandwidth of the measurement circuit. The overall tunnel rate Γ to the reservoir accumulated to the right of dot 2 is set by the barrier gate voltage V_{B3}, while the ratio of the tunnel rates $\Gamma^{\uparrow}_{\mathrm{out}}/\Gamma^{\downarrow}_{\mathrm{in}}$ can be tuned by adjusting the parameter Δ, which is the energy difference between the spin-down state and the Fermi level of the reservoir.

Thermally activated tunneling events can significantly impact the performance of energy-dependent SPAM. For example, the probability of a spin-down electron tunneling into an unoccupied state of the Fermi sea can be non-negligible. Moreover, state-preparation errors can occur when spin-up states tunnel onto the dot during the reloading period. To achieve high-fidelity spin-to-charge conversion, the Zeeman splitting E_Z must be much larger than T_e. Increasing the Zeeman splitting can suppress thermal errors but E_Z is constrained by enhanced excited-state relaxation at higher magnetic fields [31] and also by practical constraints on microwave signal generation and delivery to the device. Here, we operate at $B_{\mathrm{ext}} = 410$ mT, with $E_Z = 19.105$ GHz (79 μeV) and $T_1 = 31.5$ ms.

In addition to optimizing the ratio $E_z/k_B T_e$, the parameter Δ must also be carefully tuned to limit thermally activated tunneling events. Thermal excitation of a spin-down electron can be suppressed by increasing Δ but the trade-off is that $\Gamma^{\uparrow}_{\mathrm{out}}$ decreases and $\Gamma^{\downarrow}_{\mathrm{in}}$ increases. The decrease in $\Gamma^{\uparrow}_{\mathrm{out}}$ slows down the spin-to-charge conversion process, resulting in T_1 relaxation errors, while the

increase in $\Gamma_{\rm in}^{\downarrow}$ makes the charge-hopping events shorter and harder to detect with our 1-MHz measurement bandwidth. Therefore, the optimal Δ is large enough to suppress thermal errors and small enough to maximize the ratio $\Gamma_{\rm out}^{\uparrow}/\Gamma_{\rm in}^{\downarrow}$. The rates $\Gamma_{\rm out(in)}^{\uparrow(\downarrow)}$ are extracted by binning the tunneling times from many single-shot traces [one is shown in Fig. 2(b)] into a histogram and fitting to an exponential decay. To optimize Δ, we perform 10 000 measurements interleaving spin-up and spin-down prepared states and measure the visibility $V = F_{\uparrow} + F_{\downarrow} - 1$. Figure 2(c) shows the measurement visibility V as a function of Δ, with the optimal value $\Delta^* \approx 30\ \mu$eV resulting in $\Gamma_{\rm out}^{\uparrow} \approx \Gamma_{\rm in}^{\downarrow} \approx 20$ kHz. To counteract slow drift in the device during long quantum control sequences, we periodically recalibrate to maintain the optimal Δ^*.

With the physical parameters optimized, we now turn to the optimization of data-acquisition parameters, namely the conductance threshold $g_{\rm thr}$ and the duration of the readout window t_R. A spin-up state is registered whenever g_{S1} exceeds $g_{\rm thr}$ within the analysis time window t_R [Fig. 3(a)]. If $g_{\rm thr}$ is set too low, then background noise can lead to false positives and reduce the spin-down fidelity $F_{\downarrow}$. On the other hand, if $g_{\rm thr}$ is set too high, then we begin to miss the short near-bandwidth-limited hopping events that may not reach full amplitude, resulting in a reduced spin-up fidelity $F_{\uparrow}$. The time t_R should be long enough to catch all hopping events from spin-to-charge conversion. However, if t_R greatly exceeds the characteristic tunneling time $t_{\rm out}^{\uparrow}$, then more thermal errors will occur, limiting $F_{\downarrow}$. In larger arrays with sequential readout steps, the readout time will also need to be balanced against T_1 decay in the subsequent qubits, adding an additional constraint on t_R and the tunneling rates [13].

To optimize these parameters, we perform 10 000 measurements interleaving spin-up and spin-down prepared states using the optimized Δ^* from above. In Fig. 3(b), the measurement fidelities $F_{\uparrow(\downarrow)}$ and visibility $V = F_{\uparrow} + F_{\downarrow} - 1$ are plotted as a function of $g_{\rm thr}$, showing the optimum $g_{\rm thr}^* = 0.22\ e^2/h$. The slight negative slope at the top of the visibility curve indicates that we are near bandwidth limitations, as the very short hopping events are effectively low-pass filtered and unable to reach full amplitude. Figure 3(c) shows the measurement infidelities $1 - F$ as a function of t_R. The highest readout visibility is obtained with $t_R^* = 670\ \mu$s. Sampling beyond this time slowly increases $1 - F_{\downarrow}$ due to thermal tunneling events, which reduces the overall visibility. The step features in the 10^{-4} regime of the $1 - F_{\downarrow}$ curve are due to finite sampling. These fidelity estimates inherently include errors from both state preparation and measurement.

With all of the parameters optimized, we are able to achieve detection fidelities $> 99\%$, with $F_{\downarrow} = 99.86\% \pm 0.05\%$ and $F_{\uparrow} = 99.26\% \pm 0.12\%$ yielding an average measurement fidelity $F_M = 99.56\%$. Statistical error

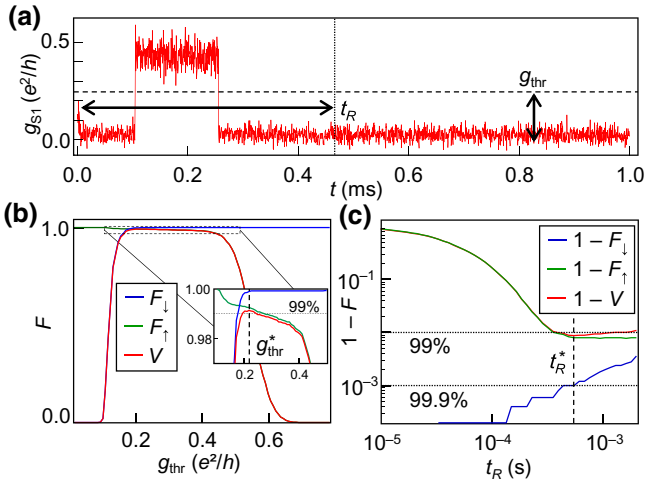

FIG. 3. Optimization of the software readout parameters. (a) A typical time series with the conductance threshold $g_{\rm thr}$ and end-of-read window t_R indicated. (b) The measurement fidelity for spin-up (spin-down) states $F_{\uparrow}$ ($F_{\downarrow}$) and the overall measurement visibility V as a function of $g_{\rm thr}$. The optimum threshold $g_{\rm thr}^*$ is indicated in the inset with a vertical dashed line. (c) The measurement infidelities plotted on a logarithmic scale as a function of t_R. The optimum end of read window t_R^* is indicated with a vertical dashed line. With both parameters optimized, we achieve $F_{\downarrow} = 99.86\%$, $F_{\uparrow} = 99.26\%$, and $V = 99.12\%$.

is estimated as one standard deviation from binomial sampling. The spin-up fidelity levels off at 99.26% due to a loss of spin information from T_1 relaxation (approximately 0.2%) and missed spin bumps caused by bandwidth limitations in the amplification chain (approximately 0.5%). Relaxation errors are calculated using the characteristic tunneling time $t_{\rm out}^{\uparrow} = 50\ \mu$s plus a 10 μs readout settling time, and T_1. The probability of missing a spin bump is $P_{\rm miss}^{\uparrow} = 1 - \dfrac{(1 - e^{(R_s^{\uparrow} - R_s^{\downarrow})/2})R_s^{\uparrow}}{(1 - e^{R_s^{\uparrow}/2})(R_s^{\uparrow} - R_s^{\downarrow})}$, where $R_s^{\uparrow} = t_s/t_{\rm out}^{\uparrow}$, $R_s^{\downarrow} = t_s/t_{\rm in}^{\downarrow}$, and $t_s = 1\ \mu$s is the sampling time [30]. We estimate an additional $P_{\rm out}^{\downarrow} = 0.06\%$ error due to thermal excitations using $P_{\rm out}^{\downarrow} = e^{-t_{\rm out}^{\downarrow}/t_R}$, where $t_{\rm out}^{\downarrow}$ is estimated from $t_{\rm out}^{\downarrow} = t_{\rm in}^{\downarrow} e^{E_z/2k_BT_e}$ [30]. Tunneling out of the spin-down state reduces the spin-down fidelity and the remaining approximately 0.1% of error is likely due to slow drift of Δ during measurement.

As limited measurement bandwidth is the biggest contributor to infidelity and a technically challenging issue to address, it is important to discuss its influence on device tuning and SPAM errors. The probability of missing an event $P_{\rm miss}^{\uparrow}$ is dependent on the ratio of the sampling rate to the tunneling rates such that we can increase both one to one and achieve the same SPAM error. Similarly, increasing the sampling rate while holding all other parameters constant would reduce $P_{\rm miss}^{\uparrow}$ proportionally. While T_1 here

is long relative to the measurement time of the qubit, for readout schemes involving serial measurements of multiple qubits, it will be important to operate with faster tunneling rates. For instance, sequential readout of two qubits with T_1 and T_e comparable to our device, and with a fidelity exceeding 99%, will require approximately a factor of 10 increase in both the bandwidth and the tunnel rates.

To minimize SPAM errors, we begin by estimating a desired tunneling rate based on the bandwidth constraints defined above. The Fermi offset, Δ, is set to halfway between the spin-down and spin-up states. The tunnel rates are tuned near their optimal values by analyzing charge-hopping data similar to Fig. 1(c) or single-shot data similar to Fig. 2(b). The analysis parameters g_{thr} and t_R can be estimated from single-shot data, with the guidance being that g_{thr} needs to be just above the noise floor and t_R should be overestimated, since the infidelity is less sensitive to t_r past the optimal stopping time. With these estimates in place, we first tune Δ to find Δ^*, as this parameter is primarily influenced by T_e. Finally, while holding Δ^* constant, we adjust the tunnel rates to minimize the infidelities shown in Fig. 3.

III. HIGH-FIDELITY SPIN CONTROL

Past experiments demonstrating high-fidelity control of LD spin qubits have generally been limited to $V \approx$ 70%–80% [10,22,32]. Recent experiments on a six-qubit device have achieved V values ranging from 93.5% to 98% [16]. Here, we demonstrate the integrated high performance of our device. Figure 4(a) shows the spin-up probability $P_\uparrow$ plotted as a function of the frequency detuning Δf from resonance (19.105 GHz) and the microwave burst length τ_R. Rabi oscillations are obtained when driving on resonance [Fig. 4(b)]. We rigorously verify high gate and SPAM fidelities using gate-set tomography (GST) protocols for single-qubit gates (I, X, Y) [33], where an X (Y) gate is a $\pi/2$ rotation performed about the X (Y) axis and I is performed by idling the qubit for the same amount of time as the X (Y) rotations. GST yields a state-preparation fidelity $\rho_0 = 99.76\% \pm 0.04\%$ and a measurement fidelity $M = 99.35\% \pm 0.1\%$, which is consistent with Fig. 3. The average single-qubit gate fidelities extracted from GST are 99.956% ±0.002%. The gate fidelity is primarily limited by incoherent noise caused by qubit dephasing ($T_2^* = 3.2$ μs, $T_2^H = 139$ μs measured using Ramsey and Hahn echo pulse sequences). Due to the modest T_2^*, the idling fidelity $F_I = 99.43\% \pm 0.036\%$ is significantly lower than the fidelities obtained during driven evolution. The error bars are 95% confidence intervals calculated in the GST analysis.

Finally, we perform IRB to estimate fidelities for the interleaved gates $(X, X^2, -X, Y, Y^2, -Y)$ [34], where a X^2 (Y^2) gate is a full π rotation about the respective axis. To obtain reliable results, we utilize $k = 200$ unique

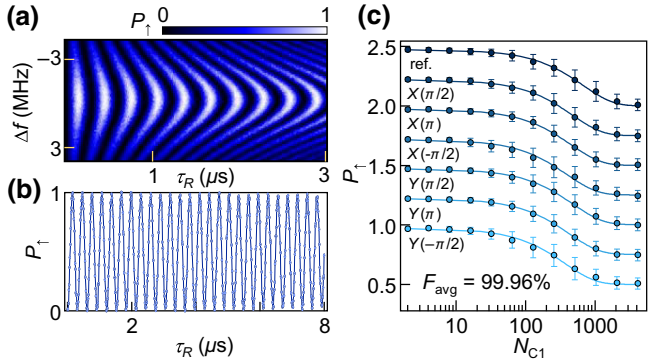

FIG. 4. Single-qubit randomized benchmarking. (a) $P_\uparrow$ as a function of the frequency detuning Δf from resonance (19.105 GHz) and τ_R. (b) High-visibility Rabi oscillations from driving the qubit on resonance. (c) The return probability $P_\uparrow$ as a function of N_{C1} for each IRB curve (including the reference) showing high-visibility, full saturation, and an average gate fidelity of 99.96%. The curves are offset by 0.25 for clarity.

sequences per point, with 100 averages. We choose $k = 200$ to obtain a rigorous gate-error estimate, as $1/f$ -noise-dominated systems see diminishing returns on the accuracy of this estimate when increasing k beyond approximately 100 [35]. Sequence lengths of up to $N_{C1} = 4096$ Clifford operations are employed to achieve full saturation of the sequence fidelity curves [Fig. 4(c)]. The average Clifford operation is composed of 1.875 single-qubit gates. The error bars on each point are the standard deviation of the fidelities for the 200 unique sequences at each point. The average gate fidelities are shown in Table I, with error bars determined using bootstrapping, a technique to randomly resample within the full data set to build statistics [36]. Retuning routines are implemented at approximately 30-min intervals during these long measurements (approximately 14 h) to correct for readout and qubit-frequency drift. Moreover, to reduce heating at the

TABLE I. Interleaved randomized benchmarking gate fidelities. The average Clifford fidelity is 99.92%, corresponding to an average gate fidelity of about 99.96%, in agreement with extracted gate fidelities. On the right, we show GST results for SPAM, identity, and gate operations X and Y with an average gate operation fidelity of 99.956%.

IRB fidelities		GST fidelities	
Gate	Fidelity (%)	Operation	Fidelity (%)
X	99.969 ± 0.004	ρ_0	99.76 ± 0.04
X^2	99.964 ± 0.003	M	99.35 ± 0.1
$-X$	99.949 ± 0.005	I	99.43 ± 0.036
Y	99.973 ± 0.004	X	99.958 ± 0.002
Y^2	99.961 ± 0.004	Y	99.954 ± 0.002
$-Y$	99.937 ± 0.005		

device, the charge-sensor excitation is turned off during qubit manipulation.

IV. CONCLUSIONS

In conclusion, our measurements show that Si spin qubits can be operated reliably with all-around high performance metrics. Optimal SPAM requires careful balancing of physical constraints with hardware constraints to minimize the loss of spin information due to spin relaxation and a finite 1-MHz measurement bandwidth. We are able to achieve measurement fidelities exceeding 99%, as verified through the analysis of single-shot readout traces and GST. GST and IRB are implemented to demonstrate average single-qubit gate fidelities exceeding 99.95% under the same operating conditions. Looking ahead, Elzerman readout of larger LD spin-qubit arrays [13,16,37,38] will require a reduction of the measurement time relative to the spin-relaxation time. Furthermore, faster readout protocols, such as those based on Pauli spin blockade, will be necessary to fully unlock the potential of feedback-based error-correction protocols and could be implemented with the measurement circuit described here [39].

ACKNOWLEDGMENTS

This work was supported by Army Research Office Grant No. W911NF-15-1-0149 and Defense Advanced Research Projects Agency Grant No. D18AC0025. The devices were fabricated in the Princeton University Quantum Device Nanofabrication Laboratory, which is managed by the Department of Physics. We acknowledge the use of Princeton's Imaging and Analysis Center, which is partially supported by the Princeton Center for Complex Materials, a National Science Foundation MRSEC program (DMR-2011750).

APPENDIX A: READOUT CIRCUIT

The readout circuit described in Fig. 1(a) achieves high-SNR charge sensing with approximately 1 MHz of bandwidth by sinking the charge-sensor current through a 20-kΩ resistor on the sample PCB. The voltage drop across the resistor is amplified with two-stages of cryogenic HEMT amplifiers (Avago ATF-38133), with the first-stage HEMT at the still plate and the second-stage HEMT at the 4 K plate. Details on the amplifier are given elsewhere [15]. Thermal isolation between the sample and the first-stage HEMT, as well as between the two amplification stages, is achieved with thin stainless-steel (SS) connections. The distance between the sample and the first-stage amplifier is reduced by using a cold finger to mount the amplifier near the sample. The output of the second stage is returned to room temperature on (Be-Cu)/SS coax with no attenuators on the lines. The input (drive) side of the circuit is delivered through stainless-steel coax with −60 dB total attenuation. At room temperature, the output of the cryoamplifiers is further amplified by a FEMTO HVA-10M-60-B voltage amplifier, before homodyne detection with a ZAD-3H+ Minicircuits mixer.

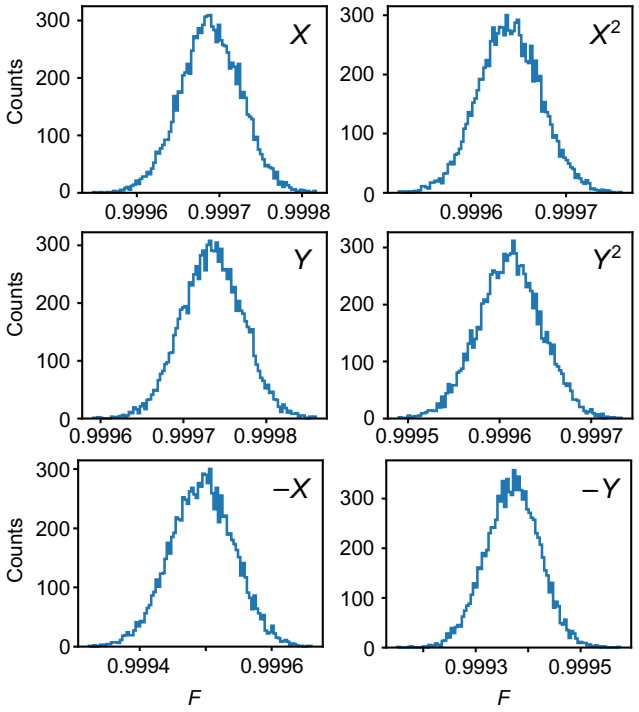

FIG. 5. Bootstrap fidelity estimates. Distributions of the 10 000 randomly resampled subsets for each of the interleaved gates. The distributions are approximately normal and the error bars reported are defined as one standard deviation.

APPENDIX B: FIDELITY ERROR-BAR ESTIMATION

Error-bar estimates for the interleaved gate fidelities are estimated using a resampling technique known as bootstrapping [40], which is a common method for estimating RB errors [36,41–43]. Bootstrapping is a statistical procedure that allows the reliable calculation of standard errors and construction of confidence intervals by generating many simulated data sets from an initial data set. Here, the main data set is a collection of randomized benchmarking decay curves for the reference and each of the interleaved gates. To collect the data, we average 100 shots for 200 unique RB sequences at each Clifford gate length N_{C1} for each of the seven curves shown in Fig. 4(c). The probability of returning to $P_{\uparrow}$ at the end of the Clifford sequence is the estimated sequence fidelity and is plotted as a function of N_{C1}. Each of the individual unique sequences k approximates the sequence fidelity for the corresponding N_{C1}. The data points in Fig. 4(c) are the average of these 200 sequence fidelities and their standard deviation is plotted as the error bar. To perform the bootstrapping analysis

on these data, we construct simulated data points by randomly choosing $K = 200$ of the unique sequences from the corresponding population. In randomly choosing these new populations, we can allow for replacement, meaning that a k can be picked more than once. From these reconstructed data points, we extract a fidelity estimate by fitting the RB decay curve. We perform this for 10 000 simulated samples and bin the extracted fidelities into histograms, as shown in Fig. 5. These histograms approximate a normal distribution and we use the standard deviation to define the error estimate. The RB error bars are one standard deviation of the gate fidelities from bootstrapping and represent the distribution of fidelity estimates that we would expect to see when repeating the RB experiments.

[1] D. Loss and D. P. DiVincenzo, Quantum computation with quantum dots, Phys. Rev. A **57**, 120 (1998).

[2] W. Ha, S. D. Ha, M. D. Choi, Y. Tang, A. E. Schmitz, M. P. Levendorf, K. Lee, J. M. Chappell, T. S. Adams, D. R. Hulbert, E. Acuna, R. S. Noah, J. W. Matten, M. P. Jura, J. A. Wright, M. T. Rakher, and M. G. Borselli, A flexible design platform for Si/SiGe exchange-only qubits with low disorder, Nano. Lett. **22**, 1443 (2022).

[3] X. Xue, *et al.*, CMOS-based cryogenic control of silicon quantum circuits, Nature **593**, 205 (2021).

[4] G. Burkard, T. D. Ladd, J. M. Nichol, A. Pan, and J. R. Petta, Semiconductor spin qubits (2021) ArXiv:2112.08863.

[5] J. R. Petta, A. C. Johnson, J. M. Taylor, E. A. Laird, A. Yacoby, M. D. Lukin, C. M. Marcus, M. P. Hanson, and A. C. Gossard, Coherent manipulation of coupled electron spins in semiconductor quantum dots, Science **309**, 2180 (2005).

[6] F. H. L. Koppens, C. Buizert, K.-J. Tielrooij, I. Vink, K. Nowack, T. Meunier, L. Kouwenhoven, and L. Vandersypen, Driven coherent oscillations of a single electron spin in a quantum dot, Nature **442**, 766 (2006).

[7] A. M. Tyryshkin, S. Tojo, J. J. L. Morton, H. Riemann, N. V. Abrosimov, P. Becker, H.-J. Pohl, T. Schenkel, M. L. W. Thewalt, K. M. Itoh, and S. A. Lyon, Electron spin coherence exceeding seconds in high-purity silicon, Nat. Mater. **11**, 143 (2012).

[8] P. W. Deelman, L. F. Edge, and C. A. Jackson, Metamorphic materials for quantum computing, MRS Bull. **41**, 224 (2016).

[9] D. M. Zajac, T. M. Hazard, X. Mi, K. Wang, and J. R. Petta, A reconfigurable gate architecture for Si/SiGe quantum dots, Appl. Phys. Lett. **106**, 223507 (2015).

[10] J. Yoneda, K. Takeda, T. Otsuka, T. Nakajima, M. R. Delbecq, G. Allison, T. Honda, T. Kodera, S. Oda, Y. Hoshi, N. Usami, K. M. Itoh, and S. Tarucha, A quantum-dot spin qubit with coherence limited by charge noise and fidelity higher than 99.9%, Nat. Nanotechnol. **13**, 102 (2018).

[11] X. Xue, M. Russ, N. Samkharadze, B. Undseth, A. Sammak, G. Scappucci, and L. M. K. Vandersypen, Quantum logic with spin qubits crossing the surface code threshold, Nature **601**, 343 (2022).

[12] A. Noiri, K. Takeda, T. Nakajima, T. Kobayashi, A. Sammak, G. Scappucci, and S. Tarucha, Fast universal quantum gate above the fault-tolerance threshold in silicon, Nature **601**, 338 (2022).

[13] A. R. Mills, C. R. Guinn, M. J. Gullans, A. J. Sigillito, M. M. Feldman, E. Nielsen, and J. R. Petta, Two-qubit silicon quantum processor with operation fidelity exceeding 99%, Sci. Adv. **8**, eabn5130 (2022).

[14] R. W. Andrews, C. Jones, M. D. Reed, A. M. Jones, S. D. Ha, M. P. Jura, J. Kerckhoff, M. Levendorf, S. Meenehan, S. T. Merkel, A. Smith, B. Sun, A. J. Weinstein, M. T. Rakher, T. D. Ladd, and M. G. Borselli, Quantifying error and leakage in an encoded Si/SiGe triple-dot qubit, Nat. Nanotechnol. **14**, 747 (2019).

[15] J. Z. Blumoff, *et al.*, Fast and High-Fidelity State Preparation and Measurement in Triple-Quantum-Dot Spin Qubits, PRX Quantum **3**, 010352 (2022).

[16] S. G. J. Philips, M. T. Madzik, S. V. Amitonov, S. L. de Snoo, M. Russ, N. Kalhor, C. Volk, W. I. L. Lawrie, D. Brousse, L. Tryputen, B. P. Wuetz, A. Sammak, M. Veldhorst, G. Scappucci, and L. M. K. Vandersypen, Universal control of a six-qubit quantum processor in silicon, Nature **609**, 919 (2022).

[17] A. G. Fowler, M. Mariantoni, J. M. Martinis, and A. N. Cleland, Surface codes: Towards practical large-scale quantum computation, Phys. Rev. A **86**, 032324 (2012).

[18] F. Borjans, X. G. Croot, X. Mi, M. J. Gullans, and J. R. Petta, Resonant microwave-mediated interactions between distant electron spins, Nature (London) **577**, 195 (2020).

[19] J. Medford, J. Beil, J. M. Taylor, S. D. Bartlett, A. C. Doherty, E. I. Rashba, D. P. DiVincenzo, H. Lu, A. C. Gossard, and C. M. Marcus, Self-consistent measurement and state tomography of an exchange-only spin qubit, Nat. Nanotechnol. **8**, 654 (2013).

[20] J. M. Elzerman, R. Hanson, L. H. W. Van Beveren, B. Witkamp, L. M. K. Vandersypen, and L. P. Kouwenhoven, Single-shot read-out of an individual electron spin in a quantum dot, Nature **430**, 431 (2004).

[21] V. Srinivasa, K. C. Nowack, M. Shafiei, L. M. K. Vandersypen, and J. M. Taylor, Simultaneous Spin-Charge Relaxation in Double Quantum Dots, Phys. Rev. Lett. **110**, 196803 (2013).

[22] X. Xue, T. F. Watson, J. Helsen, D. R. Ward, D. E. Savage, M. G. Lagally, S. N. Coppersmith, M. A. Eriksson, S. Wehner, and L. M. K. Vandersypen, Benchmarking Gate Fidelities in a Si/SiGe Two-Qubit Device, Phys. Rev. X **9**, 021011 (2019).

[23] I. T. Vink, T. Nooitgedagt, R. N. Schouten, L. M. K. Vandersypen, and W. Wegscheider, Cryogenic amplifier for fast real-time detection of single-electron tunneling, Appl. Phys. Lett. **91**, 123512 (2007).

[24] D. J. Reilly, C. M. Marcus, M. P. Hanson, and A. C. Gossard, Fast single-charge sensing with a rf quantum point contact, Appl. Phys. Lett. **91**, 162101 (2007).

[25] K. D. Petersson, J. R. Petta, H. Lu, and A. C. Gossard, Quantum Coherence in a One-Electron Semiconductor Charge Qubit, Phys. Rev. Lett. **105**, 246804 (2010).

[26] S. A. Studenikin, J. Thorgrimson, G. C. Aers, A. Kam, P. Zawadzki, Z. R. Wasilewski, A. Bogan, and A. S.

Sachrajda, Enhanced charge detection of spin qubit readout via an intermediate state, Appl. Phys. Lett. **101**, 233101 (2012).

[27] P. Harvey-Collard, B. D'Anjou, M. Rudolph, N. T. Jacobson, J. Dominguez, G. A. Ten Eyck, J. R. Wendt, T. Pluym, M. P. Lilly, W. A. Coish, M. Pioro-Ladrière, and M. S. Carroll, High-Fidelity Single-Shot Readout for a Spin Qubit via an Enhanced Latching Mechanism, Phys. Rev. X **8**, 021046 (2018).

[28] M. Pioro-Ladriere, T. Obata, Y. Tokura, Y.-S. Shin, T. Kubo, K. Yoshida, T. Taniyama, and S. Tarucha, Electrically driven single-electron spin resonance in a slanting Zeeman field, Nat. Phys. **4**, 776 (2008).

[29] E. Magesan, J. M. Gambetta, and J. Emerson, Scalable and Robust Randomized Benchmarking of Quantum Processes, Phys. Rev. Lett. **106**, 180504 (2011).

[30] D. Keith, S. K. Gorman, L. Kranz, Y. He, J. G. Keizer, M. A. Broome, and M. Y. Simmons, Benchmarking high fidelity single-shot readout of semiconductor qubits, New J. Phys. **21**, 063011 (2019).

[31] F. Borjans, D. Zajac, T. Hazard, and J. Petta, Single-Spin Relaxation in a Synthetic Spin-Orbit Field, Phys. Rev. Appl. **11**, 044063 (2019).

[32] W. Huang, C. H. Yang, K. W. Chan, T. Tanttu, B. Hensen, R. C. C. Leon, M. A. Fogarty, J. C. C. Hwang, F. E. Hudson, K. M. Itoh, A. Morello, A. Laucht, and A. S. Dzurak, Fidelity benchmarks for two-qubit gates in silicon, Nature **569**, 532 (2019).

[33] E. Nielsen, J. K. Gamble, K. Rudinger, T. Scholten, K. Young, and R. Blume-Kohout, Gate set tomography, Quantum **5**, 557 (2021).

[34] E. Magesan, J. M. Gambetta, B. R. Johnson, C. A. Ryan, J. M. Chow, S. T. Merkel, M. P. da Silva, G. A. Keefe, M. B. Rothwell, T. A. Ohki, M. B. Ketchen, and M. Steffen, Efficient Measurement of Quantum Gate Error by Interleaved Randomized Benchmarking, Phys. Rev. Lett. **109**, 080505 (2012).

[35] J. M. Epstein, A. W. Cross, E. Magesan, and J. M. Gambetta, Investigating the limits of randomized benchmarking protocols, Phys. Rev. A **89**, 062321 (2014).

[36] R. Barends, *et al.*, Superconducting quantum circuits at the surface code threshold for fault tolerance, Nature **508**, 500 (2014).

[37] D. M. Zajac, T. M. Hazard, X. Mi, E. Nielsen, and J. R. Petta, Scalable Gate Architecture for a One-Dimensional Array of Semiconductor Spin Qubits, Phys. Rev. Appl. **6**, 054013 (2016).

[38] A. Sigillito, J. Loy, D. Zajac, M. Gullans, L. Edge, and J. Petta, Site-Selective Quantum Control in an Isotopically Enriched $^{28}Si/Si_{0.7}Ge_{0.3}$ Quadruple Quantum Dot, Phys. Rev. Appl. **11**, 061006 (2019).

[39] B. M. Terhal, Quantum error correction for quantum memories, Rev. Mod. Phys. **87**, 307 (2015).

[40] B. Efron, Bootstrap methods: Another look at the jackknife, Ann. Stat. **7**, 1 (1979).

[41] E. Knill, D. Leibfried, R. Reichle, J. Britton, R. B. Blakestad, J. D. Jost, C. Langer, R. Ozeri, S. Seidelin, and D. J. Wineland, Randomized benchmarking of quantum gates, Phys. Rev. A **77**, 012307 (2008).

[42] J. P. Gaebler, A. M. Meier, T. R. Tan, R. Bowler, Y. Lin, D. Hanneke, J. D. Jost, J. P. Home, E. Knill, D. Leibfried, and D. J. Wineland, Randomized Benchmarking of Multiqubit Gates, Phys. Rev. Lett. **108**, 260503 (2012).

[43] T. J. Proctor, A. Carignan-Dugas, K. Rudinger, E. Nielsen, R. Blume-Kohout, and K. Young, Direct Randomized Benchmarking for Multiqubit Devices, Phys. Rev. Lett. **123**, 030503 (2019).